On-line Identification of the LC Product in Coupled Resonant Circuits

De Angelis, Guido; De Angelis, Alessio; Moschitta, Antonio; Carbone, Paolo; Pintelon, Rik

Published in:
IEEE Transactions on Instrumentation and measurement

DOI:
10.1109/TIM.2019.2950583

Publication date:
2020

Document Version:
Submitted manuscript

On-line Identification of the LC Product in Coupled Resonant Circuits

Guido De Angelis, Alessio De Angelis, Antonio Moschitta, Paolo Carbone, Rik Pintelon

***Abstract*—We present an in-circuit approach for estimating the LC parameter in coupled resonant circuits. The theoretical background is discussed by presenting the models and performing a numerical sensitivity analysis. The method for estimating LC is based on noisy frequency response function measurements of the coupled resonant circuit. A practical implementation is presented and employed to validate the proposed method. Experimental results show that the proposed method provides an estimate of LC with a deviation of less than 4% with respect to LCR meter measurement results.**

***Index Terms*—inductive coupling, magnetic fields, frequency response function, frequency-domain system identification**

I. Introduction

Resonant RLC circuits have gained more attention in the last decade in many fields, such as power transfer [1], Biomedical systems [2]-[4], and Magnetic Positioning Systems (MPSs) [5]-[8]. In particular, MPSs are an interesting field of application and often rely on inductively coupled sets of high-Q resonant coils, as resonance can be exploited to compensate for the distance-related attenuation and extend the system range. These systems usually measure the V_{rms} of the received signals and estimate ranges by inverting a suitable magnetic field propagation model. The usage of an equivalent circuit modeling the interaction between two coils allows the inversion of the model that requires knowledge of the parameters related to physical properties of the coupled coils. Thus, a properly characterized equivalent model can support improved accuracy, system deployment and tuning. In fact, due to fabrication tolerances, the actual characteristics of a realized coil will slightly differ from the nominal value. Consequently, if nominal values are used in the propagation model, an uncertainty source is introduced that adversely affects position measurements. Hence, accurate parametric characterization of a real system can be used as a calibration tool, improving MPSs' ranging and positioning accuracy. Moreover, since these parameters can change over time due to aging and other effects, calibration should be performed online without modifying the system hardware.

The identification of the circuit parameters can often be performed under simplifying assumptions. For instance, it was shown in [5] that the RLC circuit parameters, including the mutual inductance between the coils, depend only on the coils' relative orientation and on the distance between the coils' centers. For the purpose of estimating the position in an MPS, it was also shown that the information associated with the circuit parameters can be summarized by a constant, estimated in a preliminary calibration phase, and by the mutual inductance between the coils. It is worth noting that the estimation of the RLC circuit can be affected by various sources of uncertainty, that include parasitic effects, component tolerances, and environmental conditions [7].

In the literature, the problem of estimating offline the values of lumped components, resonant frequency, and Q-factor in RLC circuits is widely studied. In [9], the component parameters are estimated using the vector fitting algorithm based on a Least Squares approach. This algorithm processes a set of impedance measurements at several frequencies, applies vector fitting recursively, and identifies lumped component parameters. In [10], the authors estimate the inductance as a function of the physical coil parameters, i.e., diameter and number of turns. Moreover, in [11], the authors use a network analyzer to estimate the Q-factor for microwave applications. In [12], the Q-factor, the resonance frequency and the coupling coefficient of a single resonator are measured through an inductively coupled sensor. Furthermore, in [13], a sensor readout system based on impedance measurement is proposed. The system performs the impedance measurement using a capacitor discharge and a readout coil that is inductively coupled with the LC sensor. However, none of the mentioned references presents a procedure to perform an online parametric identification.

This paper is focused on the identification of the product LC in an equivalent RLC circuit that models the interaction between two inductively coupled coils. Extending the preliminary results in [14], we employ input-output voltage measurements to estimate the frequency response function (FRF) of the circuit and identify the coefficients of its transfer function using frequency-domain techniques.

The procedure described in this paper extends published results by adopting a frequency-domain system identification technique enabling estimation and monitoring of the RLC parameters in an online and in-circuit fashion. Thus, disconnection of the measured circuit is not required when applying the measurement procedure.

This paper is structured as follows: In Section II, the considered circuit is described and the proposed parametric identification procedure is illustrated, including a comparison to related approaches from the literature. Next, the background

This research activity was funded through grant PRIN 2015C37B25 by the Italian Ministry of Instruction, University and Research (MIUR), whose support the authors gratefully acknowledge

G. De Angelis is with Regione Umbria, Perugia, Italy

A. De Angelis, A. Moschitta, and P. Carbone are with the Engineering Department, University of Perugia, via G. Duranti 93, 06125 Perugia, Italy. {alessio.deangelis, antonio.moschitta, paolo.carbone}@unipg.it

R. Pintelon is with Department ELEC, Vrije Universiteit Brussel, Pleinlaan 2, B1050 Brussels, Belgium.

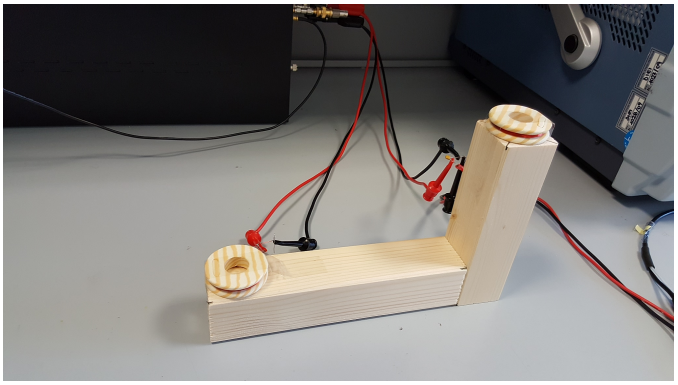

Fig. 1. Picture of the hardware setup, showing two inductively coupled coils.

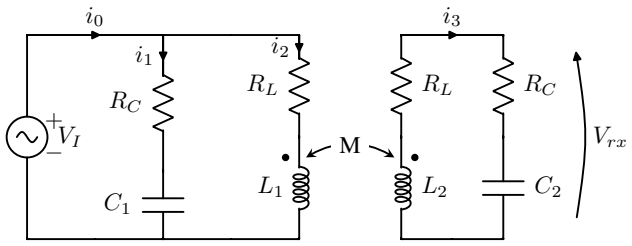

Fig. 2. Equivalent circuit of the coupled resonating coils.

theory and the derivation of the proposed identification method are introduced in Section III. Results of a numerical sensitivity analysis are discussed in Section IV. Furthermore, an experimental evaluation is presented in Section V and conclusions are drawn in Section VI.

II. Considered Circuit and Parameter Identification Method

The circuit model considered in this paper includes two inductively coupled coils, like those shown in Fig 1. The circuit parameters take into account the physical dimensions of the coils (radius, height, thickness). The relative positions of the coil centers and the coil orientations affect the value of the mutual inductance. The coils are connected to lumped capacitors thus implementing resonators.

In the general case, the resonant circuits may be connected in four configurations: parallel-parallel (PP), series-series (SS), series-parallel (SP), and parallel-series (PS). As an example, the circuit in Fig. 2 is connected in the PP configuration, since the equivalent circuit modeling the capacitor (C_1,R_C) is in parallel with the equivalent circuit of the inductor at one of the coils' sides (L_1, R_L) and because the same applies to L_2, R_L and C_2, R_C. The other configurations are presented and analyzed in the following section, where the corresponding schematic diagrams are also depicted in Fig. 7.

We make the simplifying assumption that both inductors have the same value, i.e. $L_1 = L_2 = L$, and similarly for the capacitors, i.e. $C_1 = C_2 = C$. If these values are different, then the frequency response of the overall circuit may exhibit two resonance peaks. However, the frequency response of the circuit still exhibits a single resonance peak if the Q-factor

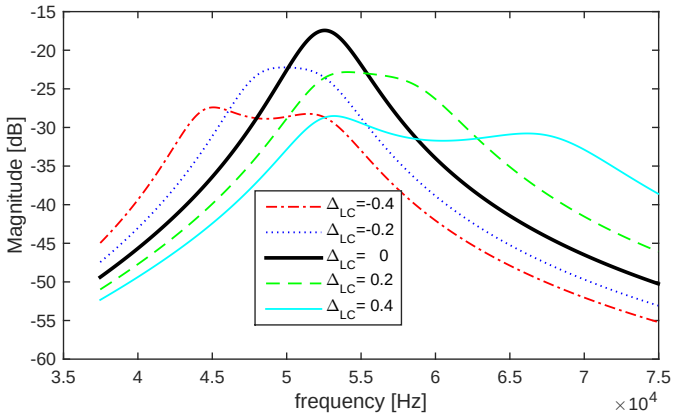

Fig. 3. Numerical simulation results of the SP configuration. Behavior of the transfer function for several values of the difference between the LC products of the two coupled resonators in the series-parallel configuration. When $\Delta_{LC} = 0.4$ and $\Delta_{LC} = -0.4$, the two resonance peaks are clearly visible.

of the resonators is of the order of magnitude of 10 and the difference between the product L_1C_1 and the product L_2C_2, which we denote as Δ_{LC}, is smaller than 20%, i.e.

$$|\Delta_{LC}| \triangleq |(L_1C_1 - L_2C_2)/L_1C_1| < 0.2.$$

This behavior is illustrated by the numerical simulation results shown in Figs. 3 and 4. The numerical simulations have been performed in the SP configuration with the following values of the circuit parameters: M = 50.0134 nH; L_1 = 30.19 μH; C_1 = 303.76 nF; R_{L1} = 0.8968 Ω; R_{C1} = 0.1851 Ω; C_2 = 311.37 nF; R_{L2} = 0.9273 Ω; R_{C2} = 0.1777 Ω. Furthermore, the simulations have been performed for different values of the L_2 parameter, from 6 μH to 53 μH, resulting in a range of Δ_{LC} values from -0.8 to 0.8. The simulated values are consistent with measurements performed on a realized prototype and reported in Section V of the present paper. Since the overall circuit exhibits a single resonance peak, it is reasonable to assume equal values of the inductors and capacitors. Thus, the presented simulation results show that the approximation is valid.

In this paper, we derive the transfer function and the expression for the LC parameter for all four possible configurations. We also report experimental estimates of the LC parameter in the PP configuration, which is widely used for magnetic positioning applications [8]. The proposed technique can be adapted for the other configurations as well.

The novelty of this paper, with respect to the other approaches recalled in Section I, consists in the application of an online frequency-domain system identification technique to the problem at hand. Accordingly, it is possible to implement online and in-circuit monitoring of the parameters for fault detection applications. The proposed online and in-circuit estimation procedure is applied while the system is operational. Such a procedure is based on input-output voltage measurements, which are performed without using external instrumentation or disconnecting the components from the circuit under test, as done for instance in [15].

The method proposed in this paper estimates the LC parameter of coupled resonant circuits using a multisine excitation.

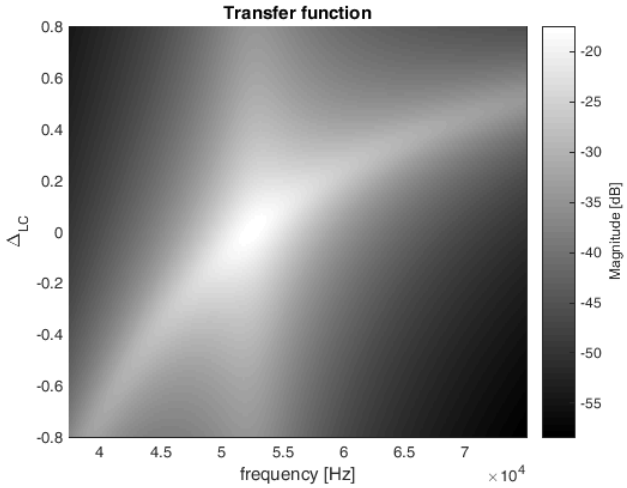

Fig. 4. Numerical simulation results of the SP configuration. Pseudo-color representation of the behavior of the transfer function for Δ_{LC} ranging from -0.8 to 0.8, obtained by varying the value of L_2 and keeping the other circuit parameters constant. It is possible to notice that a single resonance peak is present for $|\Delta_{LC}| < 0.2$, whereas two resonance peaks can be obseved for $|\Delta_{LC}| > 0.2$.

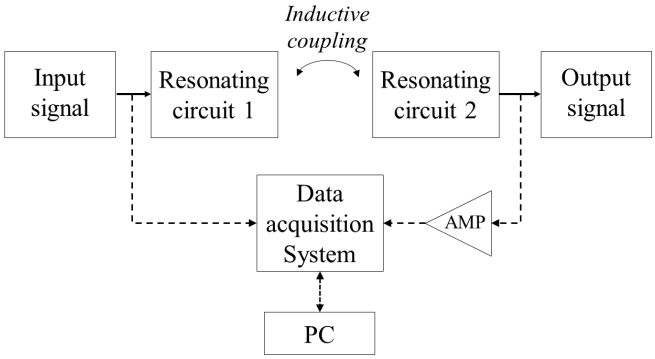

Fig. 5. Block diagram of the considered system acquiring the input-output voltage signals of a coupled-inductors resonant circuit.

Frequency-domain system identification techniques are used to identify the coefficients of the transfer function and to relate them to the LC parameter [16].

Since it is only based on input and output voltage measurements, the proposed method does not require any hardware modification of the considered RLC circuit, such as the insertion of current-measurement shunt-resistors for impedance evaluation [15], which cause Q-factor deterioration and performance degradation of the resonant circuits. Therefore, since it is an in-circuit measurement method, it can be used for online monitoring of faults that cause deviation of the circuit from its nominal characteristic, e.g. due to component aging or environmental factors.

Another possible application is the automatic tuning of coupled resonators, which could be especially beneficial for optimizing the operational range and performance of magnetic positioning or wireless power transfer systems.

Furthermore, the proposed method provides the following novelties compared with the existing in-circuit identification techniques: (i) the identification model includes noise effects on both the input and output voltage measurements, and (ii) detection and quantification of the nonlinear distortions is enabled by the usage of multisine excitations and system-identification techniques. This latter feature allows setting the validity limits of the linear approximation in the analysis of the tested circuit [16].

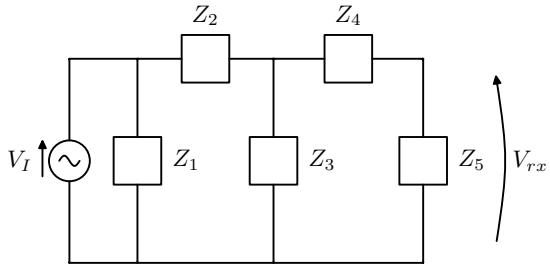

Fig. 6. Equivalent T circuit of the coupled resonating coils, showing the branch impedances Z_i.

A block diagram illustrating the architecture of the proposed measurement system is depicted in Fig. 5. The input signal provided by a signal generator to one of the two inductively-coupled resonant circuits is digitized by a data acquisition system. Simultaneously, the output signal at the other resonator is amplified by an instrumentation amplifier and digitized by a second channel of the acquisition system. The digitized signals are then transferred to a PC for further processing. In the following section, the theoretical measurement principles are described in detail.

III. Theoretical Measurement Principles

In this section, we derive the transfer function of the equivalent circuit considered, in all four configurations. Furthermore, we derive an expression of the LC parameter.

A. Analysis of the Equivalent Circuit

A schematic of the RLC circuit in the PP configuration is shown in Fig. 2. As discussed in Section II, the circuit can be analyzed under the simplifying assumptions $C = C_1 = C_2$ and $L = L_1 = L_2$ as in [5]. In particular, we can define:

$$\begin{aligned} Z_1(s) &= Z_5(s) = R_C + \frac{1}{sC} \\ Z_4(s) &= Z_2(s) = R_L + s(L - M) \\ Z_3(s) &= sM, \end{aligned} \tag{1}$$

where Z_i, with $i = 1 \dots 5$, is the impedance of each circuit branch of the equivalent T circuit depicted in Fig. 6. The parasitic resistances of the coils and the capacitors are shown as R_L and R_C, respectively. The resistor denoted as R_C is the equivalent series resistor (ESR), which is widely used in the literature to represent the losses of a capacitor.

To analyze this circuit, we derived analytical expressions and validated them using the ac analysis tool of SPICE, the widely used circuit simulator. The SPICE schematic used in the simulations, which contains resistors, capacitors, inductors,

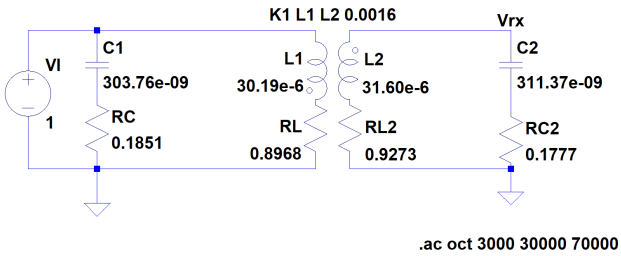

(a) PP circuit configuration.

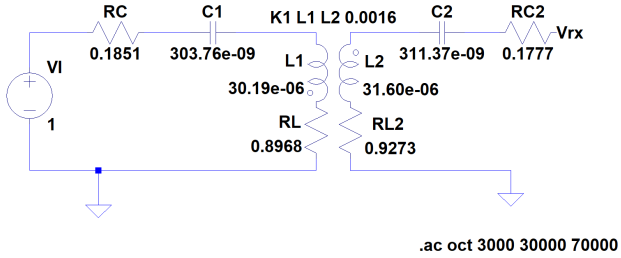

(b) SS circuit configuration.

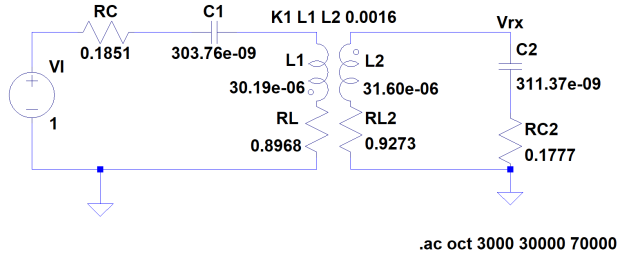

(c) SP circuit configuration.

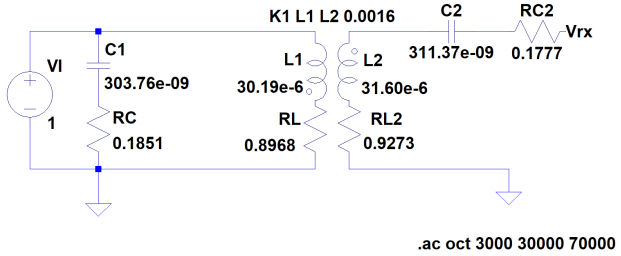

(d) PS circuit configuration.

Fig. 7. SPICE schematics of the considered circuit configurations.

mutual inductance and independent voltage sources, is shown in Fig. 7 for all circuit configurations, i.e. PP, SS, SP, and PS.

Our research is aimed at applications in the tens of kilohertz frequency range. Since parasitic capacitive effects in the inductance are often negligible at these frequencies, they are not included in the schematics shown in Fig. 7. The estimation of the parasitic effect in the inductance was discussed in [17], [18]. It is shown that the inductor behavior at very high frequencies is dominated by the parasitic capacitance effect and by other non-ideal factors [19], [20]. Simple calculations based on the model in Fig. 7 show that a parallel parasitic capacitance of a few picofarad, such as that estimated in [18], affects the inductance value by about 0.5%, when a nominal frequency of 51.5 kHz is used. The relative difference between the transfer function without parasitic capacitive effects and that obtained by considering the parasitic capacitive effects is shown in Fig. 8. It can be seen that the effect of the parasitic capacitance is negligible at the considered frequencies. Specifically, according to the curve in Fig. 8, this effect is smaller than -30 dB in the range from 2×10^5 rad/s to 4×10^5 rad/s, which contains the resonance frequency of interest of approximately 50 kHz. Furthermore, the difference between the resonance frequency with and without the parasitic capacitance is approximately 0.6% of the nominal value. The problem of estimating parasitic elements is partly addressed in Section V, whereas a more in-depth characterization of parasitics is out of the scope of this paper.

For the circuit in Fig. 6, the transfer function from V_I to V_{rx}, which we denote as $H(s)$, is given by

$$H(s) = \frac{Z_3 Z_5}{Z_4 Z_2 + Z_3 Z_2 + Z_5 Z_2 + Z_4 Z_3 + Z_5 Z_3}. \quad (2)$$

By substituting (1) in (2), we obtain

$$H(s) = -\frac{R_C C M s^2 + M s}{a_1 s^3 + a_2 s^2 + a_3 s - R_L}, \quad (3)$$

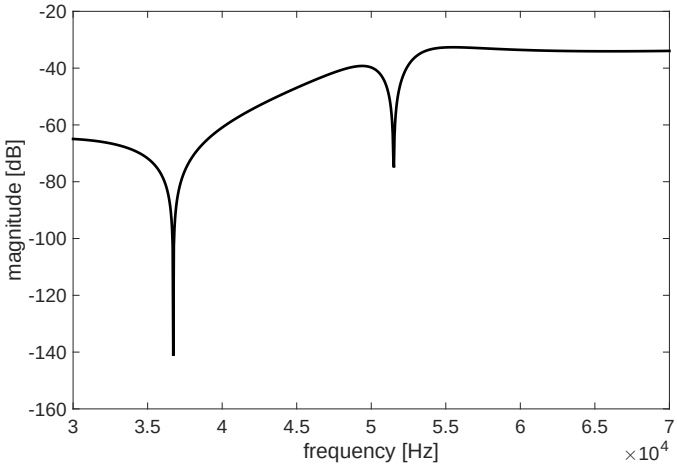

Fig. 8. Relative difference between the transfer function of the PP circuit with parasitic effect and the transfer function without parasitic effect.

where $a_1 = CM^2 - CL^2, a_2 = (-2R_L - R_C)CL, a_3 = \left(-R_L^2 - R_C R_L\right) C - L$. We compared the analytical results (3) with those provided by SPICE. This comparison is shown in Section III-C.

Note that when $L \gg M$ we can use the approximation $L - M \simeq L$, as in [5], thus obtaining

$$H(s) \cong \frac{R_C C s^2 + s}{b_1 s^3 + b_2 s^2 + b_3 s + R_L} \cdot M, \quad (4)$$

where $b_1 = CL^2, b_2 = (2R_L + R_C)CL, b_3 = (R_L^2 + R_C R_L)C + L$.

This transfer function has two zeros and three poles, since it may be written in the following form

$$H(s) \cong k \cdot \frac{s^2 + as + b}{s^3 + cs^2 + ds + e}, \quad (5)$$

where

$$k = \frac{MR_C}{L^2} \tag{6}$$

$$a = \frac{1}{CR_C} \tag{7}$$

$$b = 0 \tag{8}$$

$$c = \frac{2R_L + R_C}{L} \tag{9}$$

$$d = \frac{\left(R_L^2 + R_C R_L\right) C + L}{CL^2} \tag{10}$$

$$e = \frac{R_L}{CL^2}. \tag{11}$$

B. Analytical solution for the product LC

We may write (5) in a more convenient form by factoring the denominator as follows

$$H(s) \cong k \cdot \frac{s^2 + as}{(s+\alpha)\left(s^2 + \beta s + \gamma\right)}, \tag{12}$$

where

$$\alpha = \frac{R_L}{L} \tag{13}$$

$$\beta = \frac{R_C + R_L}{L} \tag{14}$$

$$\gamma = \frac{1}{LC}. \tag{15}$$

Notice that this model is not identifiable, i.e., it is not possible to univocally calculate the parameters M, L, C, R_C, and R_L by estimating the coefficients of the transfer function in (12). In fact, the nonlinear system of equations given by (6), (7), (13), (14), and (15), where M, L, C, R_C, and R_L are the unknowns, admits an infinite set of solutions, given by $\{\xi M_0, \xi L_0, C_0/\xi, \xi R_{C0}, \xi R_{L0}\}$, for any $\xi \in \mathbb{R}$ and $\xi \neq 0$. Here, M_0, L_0, C_0, R_{C0}, and R_{L0} are the nominal values of the circuit parameters.

In addition to the identifiability issue, another problem is the presence of strongly nonlinear functions in the expressions of the coefficients of (12). Even if the model was identifiable, solving for the unknowns would require a numerical approach, with close-to-the-solution initial values, to avoid local minima.

However, the product LC is identifiable. In fact, by measuring the FRF of the circuit and performing a parametric identification of the coefficients of (12), the product LC can be estimated by direct inversion of the γ coefficient in (15).

C. Transfer functions for the SS, SP, and PS configurations

In this section, we provide the analytical expressions of the transfer functions and the formulas for calculating the LC parameter for the SS, SP, and PS configurations. These transfer functions were obtained using the ABCD matrix method [21]. Detailed derivations are provided in the Appendix. The transfer function of the SS circuit is given by

$$H_{SS}(s) = \frac{MCs^2}{s^2CL + sC(R_L + R_C) + 1}. \tag{16}$$

In this configuration, LC is given directly by the denominator coefficient of s^2.

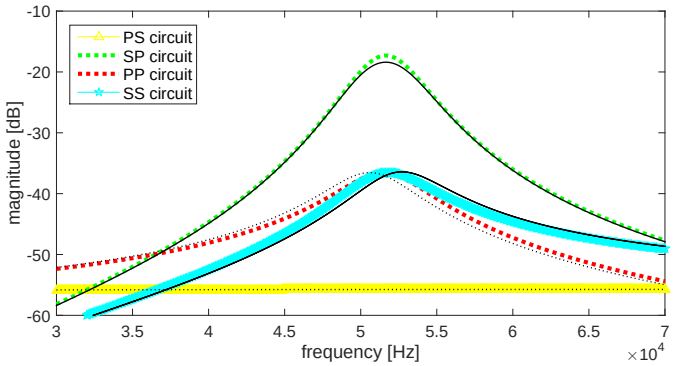

Fig. 9. Transfer function of the PS, SP, PP, and SS circuits. The color lines denote the analytical expressions, while the black lines indicate the results of the circuit simulation (SPICE).

Moreover, the SP circuit has the following transfer function

$$H_{SP}(s) = -\frac{g_3 s^3 + g_2 s^2}{f_4 s^4 + f_3 s^3 + f_2 s^2 + f_1 s - 1}, \tag{17}$$

where $g_3 = C^2 M R_C$, $g_2 = CM$, $f_4 = C^2M^2 - C^2L^2$, $f_3 = -2C^2LR_L - 2C^2LR_C$, $f_2 = -C^2R_L^2 - 2C^2R_CR_L - C^2R_C^2 - 2CL$ and $f_1 = -2CR_L - 2CR_C$. In the SP configuration, the parameter LC is given by $LC = \sqrt{g_2^2 - f_4}$.

Finally, the transfer function of the PS circuit is given by

$$H_{PS}(s) = \frac{Ms}{Ls + R_L}. \tag{18}$$

Notice that it is impossible to estimate the LC product in the PS configuration, since C does not appear in the transfer function expression. In this configuration, resonance does not occur.

By numerically evaluating the above transfer functions, we obtain the plots shown in Fig. 9. Note that, at least around the resonance frequency, the behavior of the SS and PP circuits is similar. Moreover, from Fig. 9 it can be observed that the PS circuit is not resonant, thus validating the theoretical derivation in (18). Finally, a good agreement between the curves obtained by circuit simulation and those obtained by the analytical expressions can be noticed. The small differences between those curves are due to the fact that the circuit simulations were performed with the parameter values shown in Fig. 7, whereas the analytical expressions use the simplifying assumptions $L_1 = L_2 = L$ and $C_1 = C_2 = C$.

In the remainder of the paper, we focus on the PP circuit, which is widely used in MPS applications [5]. For this configuration, we provide a numerical sensitivity analysis and experimental results in the following sections.

IV. Sensitivity Analysis

In this section, the sensitivity of the mathematical model in (3) is analyzed by analytical derivations and by numerical simulation. This analysis is useful, since it may consent to assess the tolerance requirement on the lumped components that realize the MPS's beacons and mobile nodes.

We recall that the sensitivity to the parameters is defined as the ratio between the percentage change in the transfer

function H and the percentage change in the parameter α, where α denotes any of the circuit parameters, i.e. $\alpha \in \{M,\ C,\ L,\ R_C,\ R_L\}$. Therefore, the formula for the sensitivity of H to the parameter α, denoted as S_α^H, is [22]:

$$S_\alpha^H = \left.\frac{\partial H}{\partial \alpha}\frac{\alpha}{H}\right|_{\alpha_0}, \tag{19}$$

with α_0 the nominal value of the parameter α, in our case the true value of the circuit parameter used in the simulation.

By applying (19) to the expression of $H(\cdot)$ in (3), the sensitivity associated with the M parameter is:

$$S_M^H = \left.\frac{\partial H}{\partial M}\frac{M}{H}\right|_{M_0} = \frac{S_{M,1}^H}{S_{M,2}^H}, \tag{20}$$

where

$$\begin{aligned} S_{M,1}^H =& -\left(C\,M^2 + C\,L^2\right)\,s^3 - \left(2CL\,R_L + CL\,R_C\right)s^2 \\ & - \left(C\,{R_L}^2 + C\,R_C R_L + L\right)s - R_L \\ S_{M,2}^H =& \left(C\,M^2 - C\,L^2\right)\,s^3 + \left(-2CL\,R_L - CL\,R_C\right)s^2 \\ & + \left(-C\,{R_L}^2 - C\,R_C R_L - L\right)s - R_L. \end{aligned}$$

Furthermore, for the L parameter, we have that

$$S_L^H = \frac{S_{L,1}^H}{S_{L,2}^H}, \tag{21}$$

where

$$\begin{aligned} S_{L,1}^H =& 2C\,L^2\,s^3 + \left(2CL\,R_L + CL\,R_C\right)s^2 + Ls \\ S_{L,2}^H =& \left(C\,M^2 - C\,L^2\right)\,s^3 + \left(-2CL\,R_L - CL\,R_C\right)s^2 \\ & + \left(-C\,{R_L}^2 - C\,R_C R_L - L\right)s - R_L. \end{aligned}$$

For the C parameter, the following expression applies

$$S_C^H = \frac{S_{C,1}^H}{S_{C,2}^H} \tag{22}$$

where

$$\begin{aligned} S_{C,1}^H =& -\left(C\,M^2 - C\,L^2\right)\,s^3 + 2CL\,R_L s^2 - C\,{R_L}^2 s \\ S_{C,2}^H =& \left(C^2\,M^2 - C^2\,L^2\right)\,R_C s^4 \\ & + \left(-2C^2 L\,R_C R_L - C^2 L\,{R_C}^2 + C\,M^2 - C\,L^2\right)s^3 \\ & - \left(C^2\,R_C {R_L}^2 + \left(C^2\,{R_C}^2 + 2CL\right)R_L + 2CL\,R_C\right)s^2 \\ & + \left(-C\,{R_L}^2 - 2C\,R_C R_L - L\right)s - R_L. \end{aligned}$$

Furthermore, for the R_L parameter we obtain

$$S_{R_L}^H = \frac{S_{R_L,1}^H}{S_{R_L,2}^H}, \tag{23}$$

where

$$\begin{aligned} S_{R_L,1}^H =& 2CL\,R_L s^2 + \left(2C\,{R_L}^2 + C\,R_C R_L\right)s + R_L \\ S_{R_L,2}^H =& \left(C\,M^2 - C\,L^2\right)\,s^3 + \left(-2CL\,R_L - CL\,R_C\right)s^2 \\ & + \left(-C\,{R_L}^2 - C\,R_C R_L - L\right)s - R_L. \end{aligned}$$

Finally, the expression for the R_C parameter is

$$S_{R_C}^H = \frac{S_{R_C,1}^H}{S_{R_C,2}^H}, \tag{24}$$

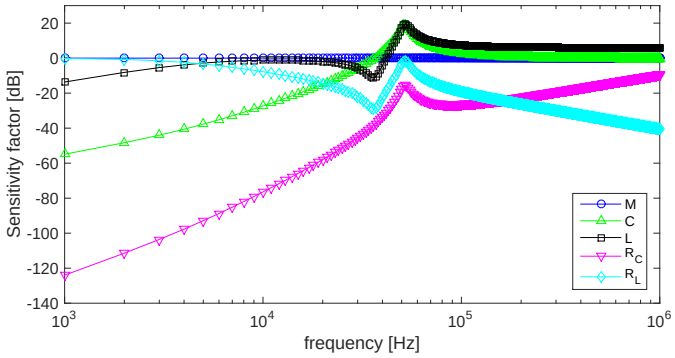

Fig. 10. Sensitivity analysis of the model in (3) to the circuit parameters.

where

$$\begin{aligned} S_{R_C,1}^H =& \left(C^2\,M^2 - C^2\,L^2\right)\,R_C s^4 \\ & - 2C^2 L\,R_C R_L s^3 - C^2\,R_C {R_L}^2 s^2 \\ S_{R_C,2}^H =& \left(C^2\,M^2 - C^2\,L^2\right)\,R_C s^4 \\ & + \left(-2C^2 L\,R_C R_L - C^2 L\,{R_C}^2 + C\,M^2 - C\,L^2\right)s^3 \\ & - \left(C^2\,R_C {R_L}^2 + \left(C^2\,{R_C}^2 + 2CL\right)R_L + 2CL\,R_C\right)s^2 \\ & + \left(-C\,{R_L}^2 - 2C\,R_C R_L - L\right)s - R_L. \end{aligned}$$

The plots shown in Fig. 10 are obtained by numerical evaluation of (20)-(24) based on the following reference values: $L = 30.887$ μH, $C = 307.54$ nF, $R_L = 0.9119$ Ω, $R_C = 0.1814$ Ω and a mutual inductance $M = 50.0134$ nH. It can be inferred that the largest sensitivities are associated with the circuit inductance and capacitance, with a reduced sensitivity to parasitic resistances.

V. Experimental Evaluation

To validate the proposed strategy for identifying the product LC, experiments were performed on a realized circuit. Such circuit consisted of the two coupled inductors depicted in Fig. 1, each connected in parallel with a lumped capacitor, according to the schematic in Fig. 2. The two air-core coils were realized by winding 20 turns of 0.25 mm diameter wire on cylindrical holders having a radius of 20 mm and a height of 3.5 mm. The resulting nominal inductance of the coils was $L_1 = L_2 = L = 29$ μH, calculated using Wheeler's formula [23]. The nominal value of the lumped capacitors was $C_1 = C_2 = C = 330$ nF. Therefore, the resonant frequency of the realized circuit was approximately 53 kHz.

A. Stepped sine excitation for FRF measurement

In order to measure the FRF of the realized circuit, a stepped sine excitation was initially used. Specifically, one of the two coils was connected to an an Agilent 33220A signal generator. This generator was configured to provide a sinusoidal waveform at a set of 81 frequencies. For each frequency, a measurement of the RMS value of the induced voltage on the other coil was performed, after amplifying the voltage at the coil by means of an AD8421 instrumentation amplifier with a gain of 40 dB. These RMS voltage measurements were performed using a Fluke 8845A Digital Multimeter.

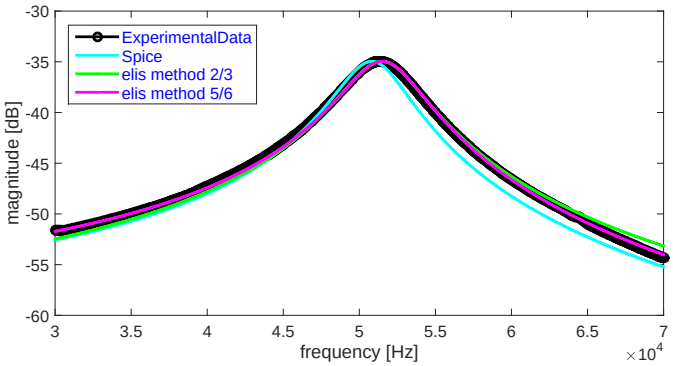

Fig. 11. Experimental results. Magnitude of the measured FRF, that simulated by Spice, that estimated using the *elis 2/3* method and the *elis 5/6* method.

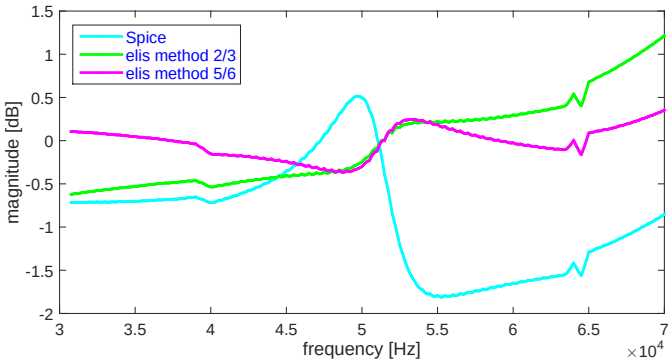

Fig. 12. Experimental results. Difference between the magnitude of the measured FRF, that simulated by Spice, that estimated using the *elis 2/3* method and the *elis 5/6* method.

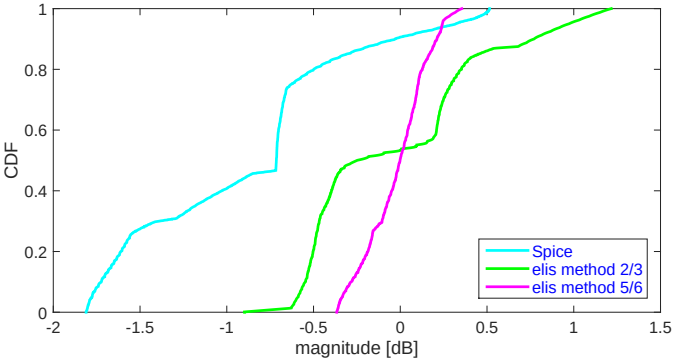

Fig. 13. Empirical CDF of the difference between the magnitude of the measured FRF, that simulated by Spice, that estimated using the *elis 2/3* method and the *elis 5/6* method.

The record of measurement results, of length 81, was subsequently resampled by interpolation, using the Matlab function *resample*, to obtain a record of 1000 values that was used for subsequent identification. During the measurement procedure, the two coils were placed on the same plane, and the distance between their centers was 10 cm. The experimental results of the FRF measurement procedure are shown in Fig. 11, where an FRF obtained by the circuit simulator Spice using the nominal values of the components is also shown.

Furthermore, the measured frequency response function data was fed to the *elis* (estimation of linear systems) algorithm for parametric system identification, which is implemented in the frequency-domain identification Matlab toolbox *fdident* [24]. The *elis* algorithm is commonly used in the literature for system identification. It solves least squares estimation problems employing the errors-in-variables model. Such a model accounts for measurement errors in both the input and the ouput of the system under test [16]. The *elis* algorithm was configured for performing a model scan, i.e. identifying a set of models differing by number of poles and zeros. The scanned numbers of zeros are from 2 to 6, whereas the scanned numbers of poles are from 3 to 6. In the following, we present results for two of the scanned models. The first model, denoted as *elis 2/3*, is defined by two zeros and three poles, which corresponds to the number of poles and zeros of the ideal model of the physical circuit in (3). The second model, denoted as *elis 5/6*, has five zeros and six poles, corresponding to the model with the smallest error within the scanned set.

The results of the identification process are presented in Fig. 11, Fig. 12, and Fig. 13. From these plots, a good agreement can be observed between the experimental data and the fitted curves, especially in the vicinity of the resonance frequency. Specifically, Fig. 12 shows a difference of less than 1.5 dB between the measured FRF and that estimated using the *elis 2/3* method and the *elis 5/6* method. For the purpose of shape comparison, here the maximum magnitude of all the FRF curves was normalized to 1. Similar observations can be obtained by the empirical cumulative density function in Fig. 13. Therefore, the feasibility of the proposed fitting strategy is validated.

B. Multisine excitation for FRF measurement

The stepped sine excitation used in the previous subsection for measuring the FRF has the main drawback of requiring a relatively long measurement time. In fact, for each of the frequency steps desired, it is necessary to perform the entire measurement procedure and sufficient time should be employed to allow for transients to vanish. To overcome this drawback, broadband excitations are often employed in practical scenarios. In particular, periodic random-phase multisine signals provide benefits such as the possibility of estimating the variance and the capability of detecting nonlinear distortions in the system [16].

For these reasons, an additional experimental test was performed, where the FRF was measured using a full random-phase multisine. The same circuit used in the previous subsection, depicted in Fig. 1, was connected to a Keysight U2331A multifunction data acquisition board, according to the block diagram of Fig. 5. The multisine excitation was generated by the on-board 12-bit DAC and two acquisition channels were used, for digitizing the input and output. Each channel was acquired with a resolution of 12 bits and a sampling rate $F_s = 300$ kSa/s, using coherent sampling with the acquisition clock synchronized with the signal generation clock.

The input signal consisted of 300 periods of a random-phase multisine synthesized using the Matlab fdident toolbox [24], with 1000 samples per period, containing all harmonics of the

fundamental frequency, which was equal to 300 Hz. The root-mean-square value of the input signal was 0.3 V. The effect of the transient was removed by discarding the first period of the acquired signals. For each of the remaining periods, the discrete Fourier transform (DFT) was computed. Then, the obtained DFT sequences were averaged and used to obtain an estimate of the FRF using the maximum likelihood estimator described in [16, chapter 2]. Such DFT sequences, which are related to repeated multisine measurements, were also used to obtain an estimate of the standard deviation of the FRF .

Two tests were performed: the first one was carried out without adding the instrumentation amplifier (INA) at the output of the system, therefore connecting the output of the receiving resonator to the acquisition board directly. The second test was performed by connecting the AD8421 INA with a gain of 40 dB to the output, thus acquiring the signal at the output of the INA. The results are shown in Fig. 14, where both the average and the standard deviation of the estimated FRF are depicted. In the figure, the nominal gain value of 40 dB is subtracted from the curve related to the INA results.

The purpose of the test carried out without the INA is to show which results can be achieved when an INA is not available in the intended application, e.g. due to low-power requirements. It follows that even in this case it is possible to estimate the transfer function in the vicinity of the resonance frequency, albeit with a degraded performance in terms of signal-to-noise ratio. Specifically, from Fig. 14, it can be seen that the two curves obtained with and without the INA are in good agreement with each other in the frequency band corresponding to the resonance peak of the system. However, the standard deviation obtained without the INA is approximately 30 dB higher than that obtained using the INA. Furthermore, the average FRF is noisy outside the resonance region, thus preventing an accurate estimation outside such region.

The FRF measurement results obtained using the multisine excitation were processed using the *elis* algorithm, obtaining the results shown in Fig. 15 and Fig. 16, for the cases without and with the INA, respectively. It is possible to notice, from Fig. 16, that the 2-zero, 3-pole model corresponding to the ideal circuit in (3) cannot accurately describe the FRF outside of the resonance region. Therefore, a more complex model is needed, with additional poles and zeros.

Such additional poles and zeros account for the effect of those parasitic components that are not included in the ideal circuit model in (3). By increasing the model order, a better fit of the experimental data is obtained, as shown by Fig. 16. This means that the parasitic components result in a non-negligible contribution in those frequency ranges that are outside of the resonance range. However, the presented experimental results prove that the simple ideal model is still usable to identify the LC parameter without a significant loss of accuracy, because the transfer function in the resonance region is correctly described even by the 2-zero, 3-pole model corresponding to the ideal circuit of (3).

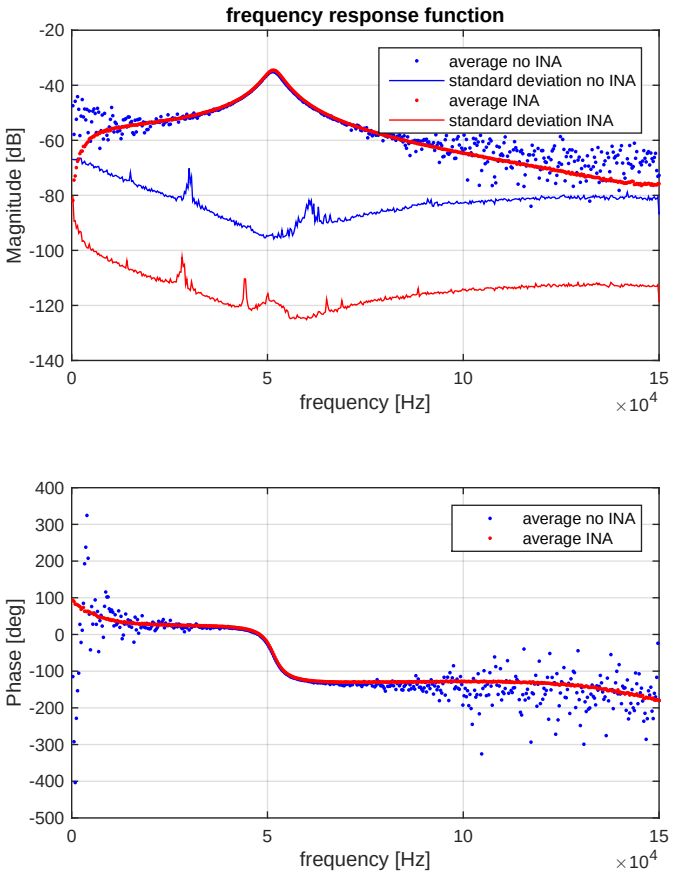

Fig. 14. Experimental results. FRF measured using a multisine excitation. The average and standard deviation are obtained by considering 300 records of the acquired signals.

C. Evaluation of the analytical expression for the product LC

The denominator of the 2-zero, 3-pole model identified in the previous subsection was factored in the form of (12), thus obtaining

$$\tilde{H}(s) = \frac{253.56s(s + 6.859 \cdot 10^5)}{(s + 5.693 \cdot 10^4)(s^2 + 3.142 \cdot 10^4 s + 1.049 \cdot 10^{11})}. \quad (25)$$

Therefore, an estimate of LC is obtained as $\hat{LC} = 1/1.049 \cdot 10^{11} = 9.5329 \cdot 10^{-12}$.

To obtain an independent validation of this result, the lumped circuit components, i.e. capacitors and inductors, were disconnected from the circuit and measured separately using an LCR meter, the Iso-Tech LCR 821, with an uncertainty of 0.05% [25]. The measurement procedure was performed at 50 kHz. The measured values are shown in Table I. It may be noticed that the measured value of C_1 differs by 7.61 nF from the measured value of C_2, while the difference between the measured values of L_1 and L_2 is 1.41 μH. Therefore, the simplifying assumptions of equal capacitance and inductance that we made in Section III-A are valid, in the experimental setup, within an approximation error of 2.4% for C and 4.46% for L. Table I also presents the comparison between the value of the product LC estimated by the proposed method and that measured using the LCR meter considering the product L_1C_1

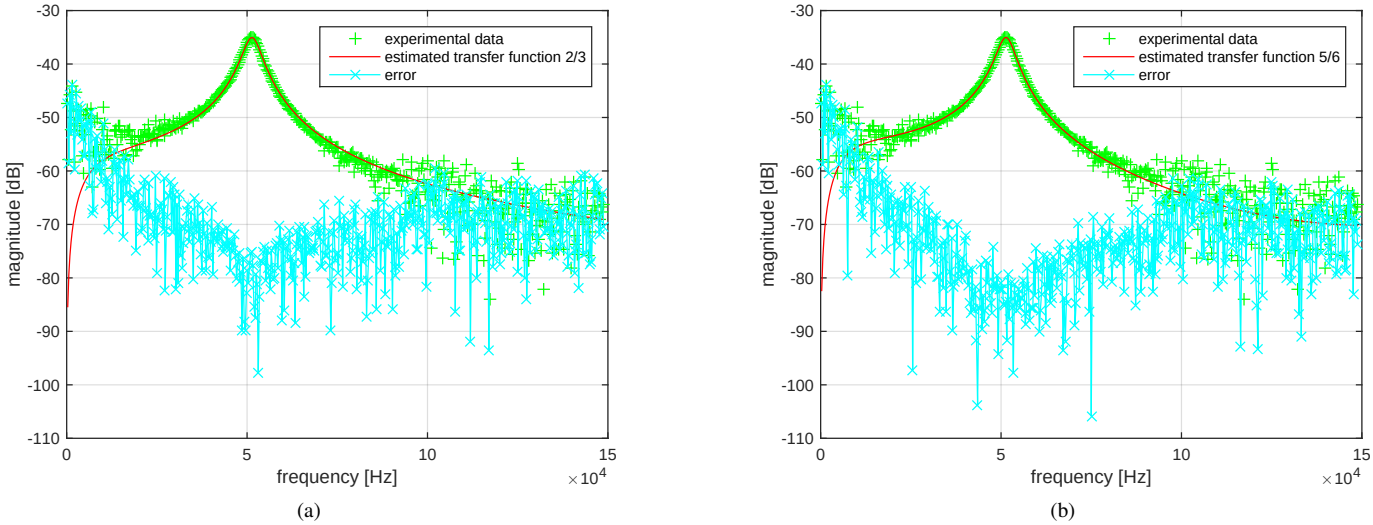

Fig. 15. Results of the parametric system identification using a multisine excitation without the INA. (a) 2-zero, 3-pole model; (b) 5-zero, 6-pole model.

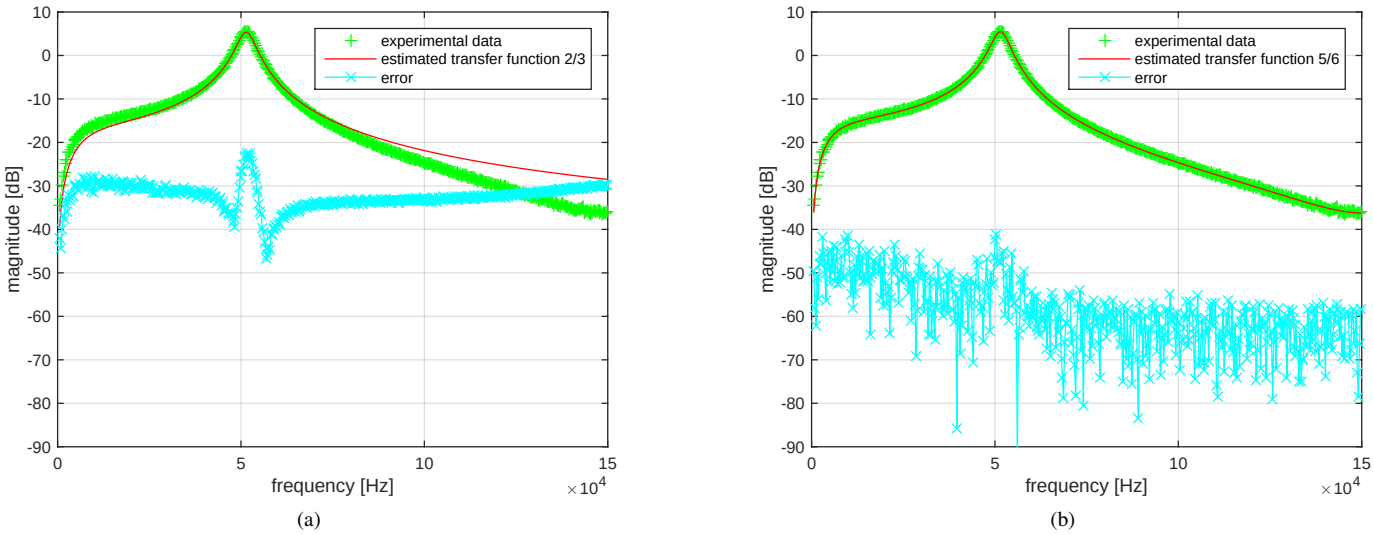

Fig. 16. Results of the parametric system identification using a multisine excitation with the INA. (a) 2-zero, 3-pole model; (b) 5-zero, 6-pole model.

and the product L_2C_2. In both cases the proposed method results in a relative error of less than 3.95%.

D. Discussion of the results

The presented experimental results prove that the proposed in-circuit identification method is feasible in a practical scenario. In particular, the results show that the LC parameter of coupled resonating circuits is estimated within an error of approximately 4% with respect to an independent validation procedure, which is performed using external instrumentation and disconnecting the individual components from the circuit. This independent validation procedure does not take into account the parasitic behaviors that arise when the circuit components are connected together during normal operation of the circuit. This fact partly explains the deviation in the estimate of the LC parameter. Moreover, with respect to this independent validation procedure, the proposed online method has the advantage of increased flexibility and possible widespread adoption in fault diagnosis scenarios.

The analysis provided in this paper assumes that only input and ouput voltages are measured. If other quantities are measured, such as input current, output current, or voltage across the individual reactive elements, then a different analysis should be carried out and possibly other circuit parameters may be identified. However, measuring currents typically requires the usage of resistive shunts that degrade the performance of the coupled circuits. Furthermore, measuring the voltage across the individual reactive elements requires additional circuitry that increases the complexity and may prevent online operation.

Potentially, the proposed in-circuit measurement method can be implemented in real time for on-line fault detection. In this context, it could be used to monitor the behavior of the LC parameter over time and measure its deviation from the nominal value. Furthermore, the method could be applied to

TABLE I
EXPERIMENTAL RESULTS. COMPARISON BETWEEN VALUES ESTIMATED ACCORDING TO THE ANALYTICAL METHOD IN SECTION III-B AND VALUES MEASURED USING AN LCR METER

	measured	estimated	error
C_1 [nF]	303.76	-	-
R_{C1} [Ω]	0.1851	-	-
L_1 [μH]	30.19	-	-
R_{L1} [Ω]	0.8968	-	-
C_2 [nF]	311.37	-	-
R_{C2} [Ω]	0.1777	-	-
L_2 [μH]	31.60	-	-
R_{L2} [Ω]	0.9273	-	-
L_1C_1 [H·F]	9.1705E-12	9.5329E-12	3.6240E-13 (3.95 %)
L_2C_2 [H·F]	9.8393E-12	9.5329E-12	-3.0640E-13 (-3.11 %)

resonance-based magnetic positioning systems to calibrate the circuit parameters automatically, thus enhancing positioning accuracy. Another possible application of the proposed method is the automatic tuning of coupled resonators, which could be especially beneficial for optimizing the operational range and performance of wireless power transfer systems.

VI. CONCLUSION

In this paper, we considered a model of an RLC tuned-resonators equivalent circuit that has numerous practical applications in the engineering field. We proposed an analytical method for identifying the product LC based on the parametric identification of the input-output voltage transfer function, which can be performed in-circuit without the need for external instrumentation. The proposed method was applied to experimental data resulting in a relative deviation of less than 4% with respect to the values measured using an LCR meter, thus demonstrating its feasibility in a practical scenario.

APPENDIX

The equivalent electrical network of two coupled resonant circuits is shown in Fig. 6 for the PP configuration. In the general case, the network modeling the two resonant circuits is decomposed into three blocks. The first block is the capacitive impedance in series or parallel with the second block, i.e., the central block, which represents the inductive impedance and the mutual inductance (modeled by a T-network). Finally, there is a third block, consisting of another capacitive impedance, which can be connected in series or parallel with the central block. In this way, it is possible to obtain diagrams that are similar to that of Fig. 6 for all four configurations. After performing such a decomposition, the circuit can be analyzed in a simple fashion by using ABCD-parameters [21].

The ABCD-parameters, which are also known as chain parameters, are usually employed for representing cascades of two-port networks. For a generic two-port network, shown in Fig. 17, the ABCD parameters are defined as follows:

$$\begin{bmatrix} V_1 \\ I_1 \end{bmatrix} = \begin{bmatrix} A & B \\ C & D \end{bmatrix} \begin{bmatrix} V_2 \\ -I_2 \end{bmatrix},$$

where V_1 is the voltage at the input port, V_2 is the voltage at the output port, I_1 is the current at the input port, and I_2 is the current at the output port.

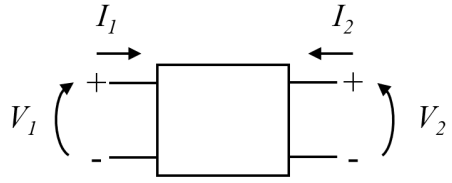

Fig. 17. Diagram of a generic two-port network, showing the convention used for defining the ABCD parameters.

The cascade of our network is resulting in the following expressions

- PS circuit: $F_{PS} = \begin{bmatrix} 1 & 0 \\ \frac{1}{Z_1} & 1 \end{bmatrix} \begin{bmatrix} A & B \\ C & D \end{bmatrix} \begin{bmatrix} 1 & Z_5 \\ 0 & 1 \end{bmatrix}$;
- SP circuit: $F_{SP} = \begin{bmatrix} 1 & Z_1 \\ 0 & 1 \end{bmatrix} \begin{bmatrix} A & B \\ C & D \end{bmatrix} \begin{bmatrix} 1 & 0 \\ \frac{1}{Z_5} & 1 \end{bmatrix}$;
- SS circuit: $F_{SS} = \begin{bmatrix} 1 & Z_1 \\ 0 & 1 \end{bmatrix} \begin{bmatrix} A & B \\ C & D \end{bmatrix} \begin{bmatrix} 1 & Z_5 \\ 0 & 1 \end{bmatrix}$;
- PP circuit: $F_{PP} = \begin{bmatrix} 1 & 0 \\ \frac{1}{Z_1} & 1 \end{bmatrix} \begin{bmatrix} A & B \\ C & D \end{bmatrix} \begin{bmatrix} 1 & 0 \\ \frac{1}{Z_5} & 1 \end{bmatrix}$;

where F_{XX} denotes the ABCD matrix of the XX circuit, with XX=$\{$PS, SP, SS, PP$\}$. Further, in a T-network, the elements of the ABCD matrix are given as follows: $A = 1 + Z_2/Z_3$, $B = Z_2 + Z_4 + (Z_2 \cdot Z_4/Z_3)$, $C = 1/Z_3$ and $D = 1 + Z_4/Z_3$. Using the definitions in (1) of the Z_i blocks, with $i = 1 \dots 5$, each transfer function H_{XX} can be obtained by inverting the first element of the corresponding F_{XX} matrix, i.e., $H_{XX}(s) = 1/F_{XX}(1,1)$ [21].

REFERENCES

[1] B. L. Cannon, J. F. Hoburg, D. D. Stancil, and S. C. Goldstein, "Magnetic resonant coupling as a potential means for wireless power transfer to multiple small receivers," *IEEE Transactions on Power Electronics*, vol. 24, no. 7, pp. 1819–1825, July 2009.

[2] A. K. RamRakhyani, S. Mirabbasi, and M. Chiao, "Design and optimization of resonance-based efficient wireless power delivery systems for biomedical implants," *IEEE Transactions on Biomedical Circuits and Systems*, vol. 5, no. 1, pp. 48–63, Feb 2011.

[3] M. Sawan, S. Hashemi, M. Sehil, F. Awwad, M. Hajj-Hassan, and A. Khouas, "Multicoils-based inductive links dedicated to power up implantable medical devices: modeling, design and experimental results," *Biomedical Microdevices*, vol. 11, no. 5, pp. 1059–1070, 2009. [Online]. Available: http://dx.doi.org/10.1007/s10544-009-9323-7

[4] E. Mattei, G. Calcagnini, F. Censi, M. Triventi, and P. Bartolini, "Numerical model for estimating rf-induced heating on a pacemaker implant during mri: Experimental validation," *IEEE Transactions on Biomedical Engineering*, vol. 57, no. 8, pp. 2045–2052, Aug 2010.

[5] G. De Angelis, A. De Angelis, A. Moschitta, and P. Carbone, "Comparison of measurement models for 3d magnetic localization and tracking," *Sensors*, vol. 17, no. 11, 2017. [Online]. Available: http://www.mdpi.com/1424-8220/17/11/2527

[6] S. Song, W. Qiao, B. Li, C. Hu, H. Ren, and M. Q. H. Meng, "An efficient magnetic tracking method using uniaxial sensing coil," *IEEE Transactions on Magnetics*, vol. 50, no. 1, pp. 1–7, Jan 2014.

[7] V. Pasku, A. De Angelis, M. Dionigi, G. De Angelis, A. Moschitta, and P. Carbone, "A positioning system based on low-frequency magnetic fields," *IEEE Transactions on Industrial Electronics*, vol. 63, no. 4, pp. 2457–2468, April 2016.

[8] V. Pasku, A. D. Angelis, G. D. Angelis, D. D. Arumugam, M. Dionigi, P. Carbone, A. Moschitta, and D. S. Ricketts, "Magnetic field-based positioning systems," *IEEE Communications Surveys Tutorials*, vol. 19, no. 3, pp. 2003–2017, March 2017.

[9] P. M. Ramos and F. M. Janeiro, "Vector fitting based automatic circuit identification," in *2016 IEEE International Instrumentation and Measurement Technology Conference Proceedings*, May 2016, pp. 1–6.

[10] M. Dionigi and M. Mongiardo, "Efficiency investigations for wireless resonant energy links realized with resonant inductive coils," in *2011 German Microwave Conference*, March 2011, pp. 1–4.

[11] K. J. Coakley, J. D. Splett, M. D. Janezic, and R. F. Kaiser, "Estimation of q-factors and resonant frequencies," *IEEE Transactions on Microwave Theory and Techniques*, vol. 51, no. 3, pp. 862–868, March 2003.

[12] R. Nopper, R. Niekrawietz, and L. Reindl, "Wireless readout of passive *LC* sensors," *IEEE Transactions on Instrumentation and Measurement*, vol. 59, no. 9, pp. 2450–2457, Sept 2010.

[13] A. Babu and B. George, "An efficient readout scheme for simultaneous measurement from multiple wireless passive *LC* sensors," *IEEE Transactions on Instrumentation and Measurement*, vol. 67, no. 5, pp. 1161–1168, May 2018.

[14] G. De Angelis, A. De Angelis, A. Moschitta and P. Carbone, "Identification of resonant circuits' parameters using weighted-least-squares fitting," in *2018 IEEE International Instrumentation and Measurement Technology Conference (I2MTC)*, May 2018.

[15] "Impedance measurement handbook. a guide to measurement technology and techniques, 6th edition," Keysight Technologies, Tech. Rep., 2016.

[16] R. Pintelon and J. Schoukens, *System Identification: A Frequency Domain Approach*. Wiley, 2012.

[17] M. Bartoli, A. Reatti, and M. K. Kazimierczuk, "Modelling iron-powder inductors at high frequencies," in *Proceedings of 1994 IEEE Industry Applications Society Annual Meeting*, vol. 2, Oct 1994, pp. 1225–1232 vol.2.

[18] A. Massarini and M. K. Kazimierczuk, "Self-capacitance of inductors," *IEEE Transactions on Power Electronics*, vol. 12, no. 4, pp. 671–676, July 1997.

[19] J. C. Hernandez, L. P. Petersen, and M. A. E. Andersen, "Low capacitive inductors for fast switching devices in active power factor correction applications," in *2014 International Power Electronics Conference (IPEC-Hiroshima 2014 - ECCE ASIA)*, May 2014, pp. 3352–3357.

[20] S. R. Joaqun Bernal, Manuel J. Freire, "Use of mutual coupling to decrease parasitic inductance of shunt capacitor filters," *IEEE TRANSACTIONS ON ELECTROMAGNETIC COMPATIBILITY*, vol. 57, no. 6, pp. 1408–1415, Dec 2015.

[21] D. A. Frickey, "Conversions between s, z, y, h, abcd, and t parameters which are valid for complex source and load impedances," *IEEE Transactions on Microwave Theory and Techniques*, vol. 42, no. 2, pp. 205–211, Feb 1994.

[22] B. C. Kuo, *Automatic Control Systems*, 5th ed. Upper Saddle River, NJ, USA: Prentice Hall PTR, 1987.

[23] H. A. Wheeler, "Simple inductance formulas for radio coils," *Proceedings of the Institute of Radio Engineers*, vol. 16, no. 10, pp. 1398–1400, Oct 1928.

[24] I. Kollar. (2004-2018) Fdident - frequency domain system identificaton toolbox for matlab. [Online]. Available: https://www.mathworks.com/products/connections/product_detail/frequency-domain-system-identification-toolbox.html

[25] *Iso-Tech LCR 800 series user manual*, https://docs-emea.rs-online.com/webdocs/0d82/0900766b80d82a9b.pdf.